

# Selective Hybrid Spin Interactions with Low Radiation Power

I. Arrazola,<sup>1</sup> E. Solano,<sup>1,2,3</sup> and J. Casanova<sup>1,2</sup>

<sup>1</sup>Department of Physical Chemistry, University of the Basque Country UPV/EHU, Apartado 644, 48080 Bilbao, Spain

<sup>2</sup>IKERBASQUE, Basque Foundation for Science, Maria Diaz de Haro 3, 48013 Bilbao, Spain

<sup>3</sup>Department of Physics, Shanghai University, 200444 Shanghai, China

We present a protocol for designing appropriately extended  $\pi$  pulses that achieves tunable, thus selective, electron-nuclear spin interactions with low-driving radiation power. Our method is general since it can be applied to different quantum sensor devices such as nitrogen vacancy centers or silicon vacancy centers. Furthermore, it can be directly incorporated in commonly used stroboscopic dynamical decoupling techniques to achieve enhanced nuclear selectivity and control, which demonstrates its flexibility.

**Introduction.**—Nanoscale nuclear magnetic resonance (NMR) emerged as a promising research field [1], with the priority goal of detecting and controlling magnetic field emitters (as nuclear spins) with high frequency and spatial resolution [2–7]. This is achieved with the help of a quantum sensor. The latter appears, e.g., when a diamond is doped with different impurities resulting in an optically active diamond sample [8]. Consequently, these impurities receive the name of color centers [9]. Among the frequent color centers one can find in diamond, we can mention, e.g., the nitrogen vacancy (NV) center [10, 11], or the silicon vacancy center [12]. These carry an electronic spin that allows fast external control with microwave (MW) radiation, while they can be initialised and measured with an optical field [13, 14]. In particular, the NV center is a prominent quantum sensor candidate owing to its long decay time (or longitudinal relaxation time) which is of the order of milliseconds at room temperature [1]. Furthermore, at low temperatures of  $\approx 3.7$  K longitudinal relaxation times that approach to  $10^3$  s have been recently reported [15]. Another error source is that affecting the quantum coherence of the sensor. This mainly appears as a consequence of the interaction among  $^{13}\text{C}$  nuclei in the diamond lattice and the NV [16]. However, with the help of dynamical decoupling (DD) techniques [17], one can efficiently remove this error source and take the coherence time  $T_2$  to the decay time  $T_1$  [17].

From a different perspective, DD techniques can be employed not only to average out magnetic fluctuations, but to selectively couple the NV to a certain target signal. The latter being classical electromagnetic radiation [18], or the hyperfine fields emitted by nuclear spins in, e.g., the diamond lattice [15], a material deposited in the diamond surface [19], or in a protein of biological interest [20]. In particular, DD techniques generate filters that allow the passage of signals with only specific frequencies [21]. It is the accuracy of this filter what determines the effectiveness of a certain DD technique and, lastly, the fidelity in detection and control over the target signal that an NV quantum sensor exerts. Continuous and pulsed (or stroboscopic) DD schemes are typically considered. The former requires to fulfill the Hartmann-Hahn double resonance condition to bridge the energy gap between the NV electron spin and, e.g., a nuclear spin target [22, 23]. The latter, however, uses the time spacing among decoupling  $\pi$  pulses

to induce a rotation frequency in the NV that matches that of the target signal [24]. Pulsed DD schemes have advantages over continuous DD methods such as the achievement of enhanced frequency selectivity by using large harmonics of the generated modulation function [24, 25]. Another advantage is the demonstrated robustness against control errors of certain pulse sequences such as those of the XY family [26, 27], or of pulse sequences including various rotation axes [28–30]. However, the use of large harmonics makes DD sequences sensitive to environmental noise, and leads to signal overlaps among different resonance branches which hinders a dependable spectral readout [25]. As we will show, these issues can be solved by applying a large static magnetic field  $B_z$ . Unfortunately, the performance of pulsed DD techniques under large  $B_z$  gets spoiled unless  $\pi$  pulses are fast, i.e. highly energetic, compared with nuclear Larmor frequencies (note that, these are proportional to  $B_z$ ). This represents a serious disadvantage, especially when DD sequences are displayed on biological samples, since fast  $\pi$  pulses require high MW power causing damage as a result of the induced heating [31].

In this Letter, we propose a design of amplitude modulated decoupling pulses that solves these problems and achieves tunable, hence highly selective, NV-nuclei interactions. The latter can be done without fast  $\pi$  pulses, i.e. with low MW power, and involving large magnetic fields. We use an NV center in diamond to illustrate our method, although this is general thus applicable to arbitrary hybrid spin systems. Furthermore, our protocol can be incorporated to standard pulsed DD sequences such as the widely used XY-8 sequence, demonstrating its flexibility.

**Model.**—We use an NV center in diamond coupled to nuclear spins and under an external MW driving. This is described by

$$H = DS_z^2 - \gamma_e B_z S_z - \sum_j \omega_L I_j^z + S_z \sum_j \vec{A}_j \cdot \vec{I}_j + H_c, \quad (1)$$

where the zero-field splitting  $D = (2\pi) \times 2.87$  GHz/T,  $\gamma_e = -(2\pi) \times 28.024$  GHz/T is the electronic gyromagnetic ratio, and  $B_z$  is applied in the NV axis (the  $z$  axis). The nuclear Larmor frequency  $\omega_L = \gamma_n B_z$  with  $\gamma_n$  the nuclear gyromagnetic ratio. For example,  $\gamma_n = (2\pi) \times 10.708$  MHz/T for  $^{13}\text{C}$  nuclei and  $(2\pi) \times 42.577$  MHz/T for protons (H).  $S_z = |1\rangle\langle 1| - |-1\rangle\langle -1|$  with  $|1\rangle$  and  $|-1\rangle$  the hyperfine lev-

els of the electronic spin state. The nuclear spin-1/2 operators  $I_j^\alpha = 1/2 \sigma_j^\alpha$  with  $\alpha = x, y, z$ , and  $\vec{A}_j$  is the hyperfine vector mediating NV-nucleus coupling. We will consider  $\vec{A}_j$  emerging from dipole-dipole interactions [16]. The control Hamiltonian  $H_c = \sqrt{2}\Omega(t)S_x \cos[\omega t - \phi]$  ( $\sqrt{2}$  is introduced for convenience) with  $S_x = \frac{1}{\sqrt{2}}(|1\rangle\langle 0| + |-1\rangle\langle 0| + \text{H.c.})$ , and  $\omega$  is the MW driving frequency on resonance with the  $|1\rangle \leftrightarrow |0\rangle$  NV spin transition. Our method requires a time-dependent modulated Rabi frequency  $\Omega(t)$  and control over the phase  $\phi$ . The latter is necessary to incorporate our method to DD sequences with alternating pulse axes. In a rotating frame with respect to (w.r.t.)  $DS_z^2 - \gamma_e B_z S_z$ , Eq. (1) reads

$$H = \sum_j \omega_j \hat{\omega}_j \cdot \vec{I}_j + \frac{\sigma_z}{2} \sum_j \vec{A}_j \cdot \vec{I}_j + \frac{\Omega(t)}{2} (|1\rangle\langle 0| e^{i\phi} + \text{H.c.}). \quad (2)$$

Here, the  $j$ th nuclear resonance frequency is  $\omega_j \approx \omega_L - \frac{1}{2}A_j^z$ , and  $\hat{\omega}_j = \vec{\omega}_j/|\vec{\omega}_j|$  with  $\vec{\omega}_j = \omega_L \hat{z} - \frac{1}{2}\vec{A}_j$  (note that  $|\vec{\omega}_j| = \omega_j$ ). Furthermore, we call  $H'_c = \frac{\Omega(t)}{2} (|1\rangle\langle 0| e^{i\phi} + \text{H.c.})$ .

Standard pulsed DD methods rely on the stroboscopic application of the MW driving (i.e. of  $H'_c$ ) leading to periodic  $\pi$  rotations in the electronic spin. This is described by the following effective Hamiltonian (in a rotating frame w.r.t.  $H'_c$ )

$$H = - \sum_j \omega_j \hat{\omega}_j \cdot \vec{I}_j + F(t) \frac{\sigma_z}{2} \sum_j \vec{A}_j \cdot \vec{I}_j, \quad (3)$$

with the modulation function  $F(t)$  taking periodically the values  $+1$  or  $-1$ , depending on the number of  $\pi$  pulses, even or odd, applied on the NV.

A common assumption of standard DD techniques is that  $\pi$  pulses are almost instantaneous, thus highly energetic. However, in real cases we deal with finite-width pulses such that, e.g., when caused by a  $H'_c$  with constant  $\Omega$ , it is required a time  $t_\pi = \frac{\pi}{\Omega}$  to produce a  $\pi$  pulse over the NV. This has adverse consequences on the NV-nuclei dynamics such as the appearance of spurious resonances [1, 32, 33], or a drastic reduction of the NMR signal sensitivity at large  $B_z$  fields [35]. However, we will demonstrate that the introduction of extended pulses with tailored  $\Omega$  avoids these problems and leads to tunable NV-nuclei interactions with low power MW radiation.

*DD with instantaneous pulses.*—Now, we consider the widely used XY-8=XYXYXYX scheme, with X (Y) a  $\pi$  pulse over the  $x$  ( $y$ ) axis. The sequential application of XY-8 on the NV leads to a periodic, even,  $F(t)$  that can be expanded in harmonic functions as  $F(t) = \sum_n f_n \cos(n\omega_M t)$ , where  $f_n = 2/T \int_0^T F(s) \cos(n\omega_M s) ds$ , and  $\omega_M = \frac{2\pi}{T}$  with  $T$  the period of  $F(t)$ , see an example of  $F(t)$  in the inset of Fig. 1 (a). In the rotating frame of  $-\sum_j \omega_j \hat{\omega}_j \cdot \vec{I}_j$ , Eq (3) is

$$H = \sum_{n,j} \frac{f_n \cos(n\omega_M t) \sigma_z}{2} \left[ A_j^x I_j^x \cos(\omega_j t) + A_j^y I_j^y \sin(\omega_j t) + A_j^z I_j^z \right], \quad (4)$$

where  $A_j^{x,y} = |\vec{A}_j^{x,y}|$  with  $\vec{A}_j^x = \vec{A}_j - (\vec{A}_j \cdot \hat{\omega}_j) \hat{\omega}_j$ ,  $\vec{A}_j^y = \hat{\omega}_j \times \vec{A}_j^x$ , and  $I_j^x = \hat{I}_j \cdot \hat{x}_j$ ,  $I_j^y = \hat{I}_j \cdot \hat{y}_j$  with  $\hat{x}_j = \vec{A}_j^x/A_j^x$  and  $\hat{y}_j = \vec{A}_j^y/A_j^y$ .

Now, we select one harmonic on the expansion of  $F(t)$  and the period  $T$ , to create a resonant interaction of the NV with a target nucleus (namely the  $k$ th nucleus). To this end, we set  $n = l$  and  $T$  such that  $l\omega_M \approx \omega_k$ . Then, after eliminating fast counter rotating terms we get

$$H \approx \frac{f_l A_k^x}{4} \sigma_z [I_k^- e^{i(\omega_k - l\omega_M)t} + \text{H.c.}] + \sum_{j \neq k} \frac{f_l A_j^x}{4} \sigma_z [I_j^- e^{i(\omega_j - l\omega_M)t} + \text{H.c.}] + \sum_{n \neq l} \sum_j \frac{f_n A_j^x}{4} \sigma_z [I_j^- e^{i(\omega_j - n\omega_M)t} + \text{H.c.}]. \quad (5)$$

High fidelity nuclear spin detection at the  $l$ th harmonic implies that with the resonance condition

$$l\omega_M = l \frac{2\pi}{T} = \omega_k, \quad (6)$$

one would get an NV- $k$ th nucleus resonant interaction while any other term in (5) is neglected. Here, the resonant term is  $f_l A_k^x / 4 \sigma_z I_k^x$ , see first line in Eq. (5), while detuned contributions (those in second and third lines) average out by invoking the rotating wave approximation (RWA). More specifically, at the resonance, we can get rid of the second line in Eq. (5) if

$$|\omega_j - \omega_k| \gg f_l A_j^x / 4. \quad (7)$$

Detuned contributions corresponding to harmonics with  $n \neq l$  are in the third line of Eq. (5), and can be neglected if

$$|\omega_j - n/l\omega_k| \approx \omega_L(l - n)/l \gg f_n A_j^x / 4. \quad (8)$$

To strengthen condition (7), one can reduce the value of  $f_l$  by selecting a large harmonic (see later), while condition (8) applies better for large values of  $B_z$  since  $\omega_L \propto B_z$ .

Assuming instantaneous pulses, standard symmetric DD sequences with a constant  $\Omega$  [26–28] lead to  $|f_l| = \frac{4}{\pi l}$  for  $l$  odd, and  $f_l = 0$  for  $l$  even. Thus, large harmonics (i.e. those with large  $l$ ) reinforce condition (7) as they lead to a smaller value of  $f_l$ . In Fig. 1 we compute the signal (black-solid) corresponding to the NV observable  $\langle \sigma_x \rangle$  in a diamond sample that contains  $150^{13}\text{C}$  nuclei. In order to obtain enough spectral resolution we will use large harmonics. Figure 1 (a) shows the harvested signal for  $l = 13$  and  $l = 15$ , as well as the theoretically expected values for  $\langle \sigma_x \rangle$  (triangles for  $l = 13$  and circles for  $l = 15$ ) that appear when perfect single nuclear addressing is considered in the numerics [36]. We can observe that the computed signal does not match with these ideal expected values. This is a consequence of using large harmonics since, for large values of  $l$ , the period  $T = 2\pi l / \omega_k$  and the spacing between  $\pi$  pulses grows, see the inset in Fig. 1(a), which spoils the efficient elimination of the static  $\sigma_z A_j^z I_j^z$  terms in Eq. (4) by the RWA. In the inset of Fig. 1 (a) we can see a sketch of the elementary pulse structure that we repeatedly apply to get the signals in Fig. 1 (a), red vertical blocks are instantaneous  $\pi$  pulses, while its associated  $F(t)$  function is in blue. To operate

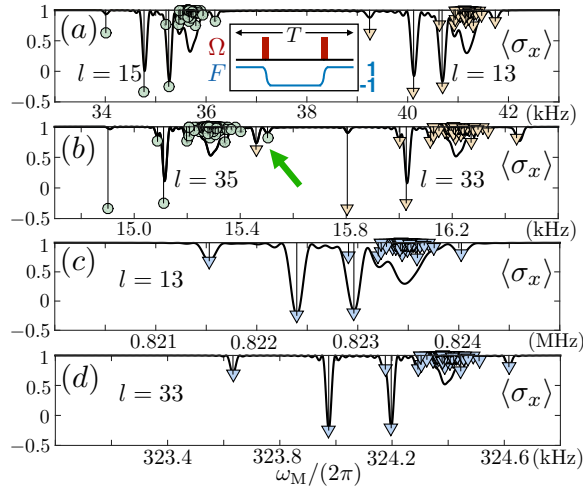


FIG. 1. Signal (black-solid) harvested with instantaneous  $\pi$  pulses and  $B_z = 500$  G in (a), (b), and  $B_z = 1$  T in (c), (d). Circles and triangles are the theoretically expected values for  $\langle \sigma_x \rangle$ . In (a) we select  $l = 13$  and  $l = 15$  and their signals are clearly separated. Inset, two-pulse block (red) used for computing signals. Below, the corresponding  $F(t)$  (blue). We repeat this block 20 times in (a) and (b), and 400 times in (c) and (d). In (b) we use  $l = 33$  and  $l = 35$ , we can observe a first spectral overlap (green arrow) that mixes peaks corresponding to different harmonics. In (c) and (d), the spectral overlap is removed as a consequence of a larger  $B_z$ , while the signal (black-solid) matches the theoretically expected values. Final sequence time is  $\approx 0.5$  ms for (a) and (c), and  $\approx 1.2$  ms for (b) and (d).

with even larger harmonics to obtain improved spectral resolution introduces additional problems such as spectral overlaps. These appear when the signal associated to a certain harmonic contains resonance peaks corresponding to other harmonics. In Fig. 1 (b) it can be observed (green arrow) how a resonance peak of  $l = 35$  (green circle) is mixed with the signal of  $l = 33$  (orange triangle). This is an additional disadvantage since the interpretation of the spectrum gets challenging.

Condition (8) is strengthened by the use of a large magnetic field as  $\omega_L \propto B_z$ , which also implies a larger resonance frequency (namely  $\omega_k$ ) for each nucleus. In this respect, note that addressing large  $\omega_k$  is also beneficial since the period  $T$  of the sequence and the interpulse spacings are smaller ( $T = 2\pi l / \omega_k$ ) turning into a better cancellation of the  $\sigma_z A_j^z I_j^z$  terms by DD. In Fig. 1 (c) and (d), we use  $B_z = 1$  T and the spectral overlap gets removed, while the computed spectrum matches with the theoretically expected signal (blue triangles).

Unfortunately, to consider  $\pi$  pulses as instantaneous in situations with a large  $B_z$  is not correct, since nuclei have time to evolve during the execution of  $\pi$  pulses leading to an uncontrolled signal drop [35]. In this manner, if one cannot deliver a huge MW power to the sample, the results in Fig. 1 (c) and (d) are not achievable.

*A solution with extended pulses.*—In any practical situation  $\pi$  pulses are finite, thus the value of  $f_l = 2/T \int_0^T F(s) \cos(l\omega_M s) ds$  has to be computed by considering the intrapulse contribution. This is (for a generic  $m$ th pulse)

$2/T \int_{t_m}^{t_m+t_\pi} F(s) \cos(l\omega_M s) ds$ , with  $t_\pi$  being the  $\pi$  pulse time and  $t_m$  the instant we start applying MW radiation, see Fig. 2 (a). In addition, the continuous  $F(s)$  functions must hold the following conditions: Outside the  $\pi$  pulse region  $F(t) = \pm 1$ , while  $F(t)$  is bounded as  $-1 \leq F(t) \leq 1 \forall t$ .

Now, we present a design for  $F(t)$  that satisfies the above conditions, cancels intrapulse contributions, and leads to tunable NV-nuclei interactions. In particular, for the  $m$ th pulse

$$F(t) = \cos[\pi(t - t_m)/t_\pi] + \sum_k \alpha_k(t) \sin[k\omega_M(t - t_p)]. \quad (9)$$

Here, the  $\alpha_k(s)$  are functions to be adjusted (see later) and  $t_p = t_m + t_\pi/2$  is the central point of the  $m$ th pulse, Fig. 2 (a). We modulate  $F(s)$  in the intrapulse region such that (for the  $m$ th pulse)  $\int_{t_m}^{t_m+t_\pi} F(s) \cos(l\omega_M s) ds = 0$ , i.e. it cancels the intrapulse contribution. Once  $F(t)$  is chosen, one can find the function  $\Omega(t)$  that generates  $F(t)$  with the formula  $\Omega(t) = \frac{\partial}{\partial t} \arccos[F(t)]$  [36]. Now, the value of the  $f_l$  coefficient obtained with the *modulated*  $F(t)$  (from now on denoted  $f_l^m$ ) depends only on the integral out of the  $\pi$  pulse region. This can be calculated leading to the following result [36]

$$f_l^m = \frac{4}{\pi l} \cos\left(\pi l \frac{t_\pi}{T}\right) \sin(\pi l/2). \quad (10)$$

Then, by simply modifying the ratio between  $t_\pi$  (the extended  $\pi$  pulse length) and  $T$  we can select the final value of  $f_l^m$  and, consequently, achieve tunable NV-nuclei interactions. According to Eq. (10),  $f_l^m$  can be taken to any amount between  $-\frac{4}{\pi l}$  and  $\frac{4}{\pi l}$ , see solid-black curve in Fig. 2 (b) for the case of  $l = 13$ . In addition, as a consequence of the periodic character of Eq. (10), one can get an arbitrary value (between  $-\frac{4}{\pi l}$  and  $\frac{4}{\pi l}$ ) for  $f_l^m$  even with large  $t_\pi$ . This implies extended  $\pi$  pulses, thus low delivered MW power. On the contrary, for standard  $\pi$  pulses in the form of *top-hat* functions (i.e. usual  $\pi$  pulses generated with constant  $\Omega$ ) one can find  $f_l \equiv f_l^{\text{th}} = \frac{4 \sin(\pi l/2) \cos[\pi l t_\pi/T]}{\pi l (1 - 4 l^2 t_\pi^2/T^2)}$ , see [36]. Unlike  $f_l^m$ , the expression for  $f_l^{\text{th}}$  shows a decreasing fashion for growing  $t_\pi$ . Note that  $|f_l^{\text{th}}| \propto [t_\pi/(T/l)]^{-2}$ . The behaviour of  $f_l^{\text{th}}$  can be observed in Fig. 2 (b), curve over the yellow area. Hence, standard top-hat pulses cannot operate with a large  $t_\pi$ , as this leads to a strong decrease of  $f_l^{\text{th}}$ , thus to signal loss.

To show the performance of our theory, we select, e.g., a gaussian form for  $\alpha_1(t) = a_1 e^{-(t-t_p)^2/2c^2}$  and set  $\alpha_k(t) = 0, \forall k > 1$ . See one example of a modulated  $F(t)$  in Fig. 2 (a) (solid-blue) as well as the behavior of  $F(t)$  in case common top-hat  $\pi$  pulses are used (solid-black). Note that other  $\alpha_k(t)$  functions satisfying the conditions for  $F(t)$  are also allowed. Once we choose the  $t_\pi$ ,  $l$ , and  $c$  parameters that will define the shape of  $F(t)$ , we select the remaining constant  $a_1$  such that it cancels the intrapulse contribution, i.e.  $\int_{t_m}^{t_m+t_\pi} F(s) \cos(l\omega_M s) ds = 0$ . By inspecting Eq. (9) one finds that a natural fashion for  $a_1$  is

$$a_1 = - \frac{\int_{t_m}^{t_m+t_\pi} \cos[\pi(s - t_m)/t_\pi] \cos(l\omega_M s) ds}{\int_{t_m}^{t_m+t_\pi} e^{-\frac{(s-t_p)^2}{2c^2}} \sin[l\omega_M(s - t_p)] \cos(l\omega_M s) ds}. \quad (11)$$

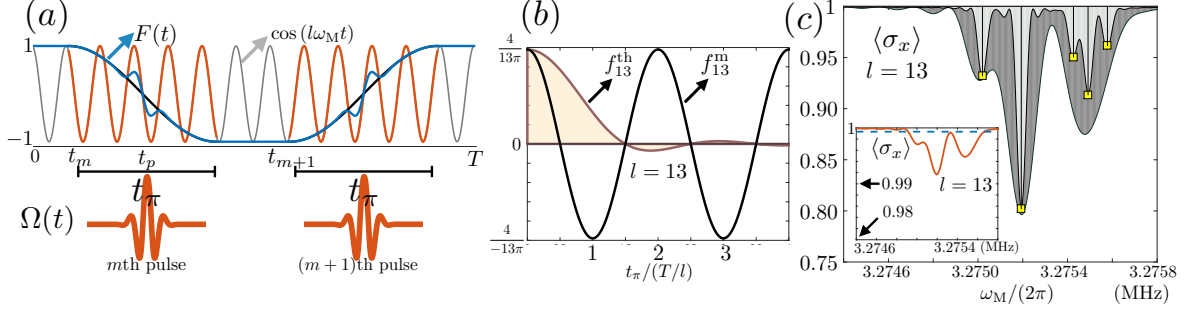


FIG. 2. (a) Upper panel, one period of the  $F(t)$  function (solid-blue) including the modulated intrapulse behavior, as well as the  $\cos(l\omega_M t)$  function. Extended  $\pi$  pulses span during  $t_\pi$  (this is the intrapulse region that appears marked in red). In this example,  $l = 13$  and  $t_\pi \approx 4.5 \times (T/l)$ . Solid-black, behavior of  $F(t)$  in case standard top-hat pulses are applied. Bottom panel, train of modulated  $\Omega(t)$  leading to  $F(t)$ . Note that, between  $\pi$  pulses  $\Omega(t) = 0$ . (b)  $f_l^m$  (black-solid) and  $f_l^th$  (curve on the yellow area) for  $l = 13$  as a function of the ratio  $t_\pi/(T/l)$  for  $l = 13$ . (c)  $\langle \sigma_x \rangle$  signals (curves over dark and clear areas) for the conditions discussed in the main text. Inset,  $\langle \sigma_x \rangle$  signals computed with top-hat pulses (see main text for details). For all numerical simulations in (c) we assume a 1% of error in the applied  $\Omega(t)$  [41].

In Fig. 2 (c) we have simulated a sample containing 5 protons at an average distance from the NV of  $\approx 2.46$  nm. The following numerical simulations have been performed starting from Eq. (2) without doing further assumptions. The 5-H target cluster has the hyperfine vectors  $\vec{A}_1 = (2\pi) \times [-1.84, -3.19, -11.02]$ ,  $\vec{A}_2 = (2\pi) \times [2.38, 5.04, -8.78]$ ,  $\vec{A}_3 = (2\pi) \times [8.09, 2.66, -1.02]$ ,  $\vec{A}_4 = (2\pi) \times [4.26, 2.46, 3.48]$ , and  $\vec{A}_5 = (2\pi) \times [4.07, 1.00, -7.09]$  kHz. We simulated two different sequences using our extended  $\pi$  pulses leading to two signals, both computed under a large magnetic field  $B_z = 1$  T. Vertical panels with yellow squares in this figure mark the theoretically expected resonance position and signal contrast. In the first computed signal, curve over dark area in Fig. 2 (c), we display a XY-8 sequence where each X (Y) extended pulse corresponds to  $\phi = 0$  ( $\phi = \pi/2$ ). More importantly, the modulated Rabi frequency in  $H'_c$  has been selected in such a way that it leads to  $f_{13}^m = 4\pi/13 = 0.0979$  for the  $l = 13$  harmonic (note this corresponds to the maximum possible value of  $f_{13}^m$ ) with a pulse length  $t_\pi = 6 \times (T/l)$ . In addition, we take the width of the Gaussian function  $\alpha_1(t)$  as  $c = 0.07t_\pi$ . The scanning frequency  $\omega_M$  spans around  $\gamma_H B_z/l$  for  $l = 13$ , see horizontal axis in Fig. 2 (c). After repeating the XY-8 sequence a number  $N = 400$  times, i.e. 3200 extended  $\pi$  pulses have been applied leading to a final sequence time of  $t_f \approx 0.488$  ms, we get the signal over the dark area in Fig. 2 (c). As we can observe in Fig. 2 (c), this sequence is not able to resolve all individual nuclear resonances of the 5-H cluster.

To overcome this situation, we make use of the tunability of our method, and simulate a second sequence using extended  $\pi$  pulses leading to the signal over the clear area in Fig. 2 (c). This has been computed by selecting a smaller value for  $f_{13}^m = 0.0979/3 = 0.0326$  which is achieved with  $t_\pi \approx 6.4 \times (T/l)$ , i.e. a slightly longer extended  $\pi$  pulse than in the preceding situation, and  $c = 0.07t_\pi$ . As the  $f_{13}^m$  coefficient is now smaller, we have repeated the XY-8 sequence a number  $N = 400 \times 3$  times (9600 pulses) to get the same contrast than in the previous case. Here, the final time of the sequence is  $t_f \approx 1.5$  ms. Note that we could also select a shorter se-

quence. As we observe in Fig. 2 (c), our method faithfully resolves each resonance in the 5-H cluster, and reproduces the theoretically expected signal contrast. It is noteworthy to comment that the tunability offered by our method will be of help for different quantum algorithms with NV centers [37–40].

**MW power and nuclear signal comparison.**—In the inset of Fig. 2 (c) we plot the signals one would get by using standard top-hat pulses with the same average power than our extended pulses in Fig. 2 (c). Here, we will use that the energy of each top-hat and extended  $\pi$  pulse,  $E^{top-hat}(t_\pi)$  and  $E^{extended}(t_\pi)$ , is  $\propto \int \Omega^2(s)ds$  where the integral extends during the  $\pi$  pulse duration (top-hat or extended). For an explicit derivation of the energy relations see [36]. In particular, the solid-orange signal in the inset has been computed with a XY-8 sequence containing 3200 top-hat  $\pi$  pulses with a constant  $\Omega \approx (2\pi) \times 18.2$  MHz. For this value of  $\Omega$ , each top-hat  $\pi$  pulse contains the same average power than each extended  $\pi$  pulse used to compute the signal over dark area in Fig. 2 (c), i.e.  $E^{top-hat}(t_\pi) = E^{extended}(t_\pi)$ . Unlike our method, the sequence with standard top-hat  $\pi$  pulses produces a signal with almost no-contrast. Note that the vertical axis of inset in Fig. 2 (c) has a maximum depth value of 0.98 and the maximum contrast achieved with top-hat pulses is smaller than 0.99. The dashed signal in the inset has been obtained with top-hat  $\pi$  pulses with  $\Omega \approx (2\pi) \times 4.68$  MHz. Again, this is done to assure we use the same average power than the sequence leading to the curve over the clear area in Fig. 2 (c). In this last case we observe that the signal harvested with standard top-hat  $\pi$  pulses does not show any appreciable contrast. These results indicate that our method using pulses with modulated amplitude is able to achieve tunable electron nuclear interactions, while regular top-hat pulses with equivalent MW power fail to resolve those interactions.

**Conclusion.**—we have presented a general method to design extended  $\pi$  pulses which are energetically efficient, and incorporable to stroboscopic DD techniques such as the widely used XY-8 sequence. Our method allows to obtain tunable interactions, hence selective, among an NV quantum sensor and

nuclear spins at large static magnetic fields which represents optimal conditions for nanoscale NMR.

Authors acknowledge financial support from Spanish MINECO/FEDER FIS2015-69983-P, Basque Government IT986-16, as well as from QMiCS (820505) and OpenSuperQ (820363) of the EU Flagship on Quantum Technologies. J.C. acknowledges support by the Juan de la Cierva grant IJCI-2016-29681. I. A. acknowledges support to the Basque Government PhD grant PRE-2015-1-0394. This material is also based upon work supported by the U.S. Department of Energy, Office of Science, Office of Advanced Scientific Computing Research (ASCR), Quantum Algorithms Teams project under field work proposal ERKJ335.

- 
- [1] C. L. Degen, F. Reinhard, and P. Cappellaro, *Rev. Mod. Phys.* **89**, 035002 (2017).
  - [2] L. Rondin, J. P. Tetienne, T. Hingant, J. F. Roch, P. Maletinsky and V. Jacques, *Rep. Prog. Phys.* **77**, 056503 (2014)
  - [3] S. Schmitt, T. Gefen, F. M. Stürner, T. Unden, G. Wolff, C. Müller, J. Scheuer, B. Naydenov, M. Markham, S. Pezzagna, J. Meijer, I. Schwarz, M. B. Plenio, A. Retzker, L. P. McGuinness, and F. Jelezko, *Science* **356**, 832 (2017).
  - [4] J. M. Boss, K. S. Cujia, J. Zopes, and C. L. Degen, *Science* **356**, 837 (2017).
  - [5] D. R. Glenn, D. B. Bucher, J. Lee, M. D. Lukin, H. Park, and R. L. Walsworth, *Nature* **555**, 351 (2018).
  - [6] J. Zopes, K. Herb, K. S. Cujia, and C. L. Degen, *Phys. Rev. Lett.* **121**, 170801 (2018).
  - [7] J. Zopes, K. S. Cujia, K. Sasaki, J. M. Boss, K. M. Itoh, and C. L. Degen, *Nat. Commun.* **9**, 4678 (2018).
  - [8] J. Walker, *Rep. Prog. Phys.* **42**, 1605 (1979).
  - [9] I. Aharonovich, S. Castelletto, D. A. Simpson, C.-H. Su, A. D. Greentree, and S. Praver, *Rep. Prog. Phys.* **74**, 076501 (2011).
  - [10] M. W. Doherty, N. B. Manson, P. Delaney, F. Jelezko, J. Wrachtrup, and L. C. L. Hollenberg, *Phys. Rep.* **528**, 1 (2013).
  - [11] D. Suter and F. Jelezko, *Prog. Nucl. Magn. Reson. Spectrosc.* **98**, 50 (2017).
  - [12] L. J. Rogers, K. D. Jahnke, M. H. Metsch, A. Sipahigil, J. M. Binder, T. Teraji, H. Sumiya, J. Isoya, M. D. Lukin, P. Hemmer, and F. Jelezko, *Phys. Rev. Lett.* **113**, 263602 (2014).
  - [13] R. Schirhagl, K. Chang, M. Loretz, and C. L. Degen, *Annu. Rev. Phys. Chem.* **65**, 83 (2014).
  - [14] Y. Wu, F. Jelezko, M. B. Plenio, and T. Weil, *Angew. Chem.* **55**, 6586 (2016).
  - [15] M. H. Abobeih, J. Cramer, M. A. Bakker, N. Kalb, M. Markham, D. J. Twitchen, and T. H. Taminiau, *Nat. Commun.* **9**, 2552 (2018).
  - [16] J. R. Maze, J. M. Taylor, and M. D. Lukin, *Phys. Rev. B* **78**, 094303 (2008).
  - [17] A. M. Souza, G. A. Álvarez, and D. Suter, *Phil. Trans. R. Soc. A* **370**, 4748 (2012).
  - [18] J. M. Taylor, P. Cappellaro, L. Childress, L. Jiang, D. Budker, P. R. Hemmer, A. Yacoby, R. Walsworth, and M. D. Lukin, *Nat. Phys.* **4**, 810 (2008).
  - [19] C. Müller, X. Kong, J.-M. Cai, K. Melentjević, A. Stacey, M. Markham, D. Twitchen, J. Isoya, S. Pezzagna, J. Meijer, J. F. Du, M. B. Plenio, B. Naydenov, L. P. McGuinness, and F. Jelezko, *Nat. Commun.* **5**, 4703 (2014).
  - [20] Z.-Y. Wang, J. F. Haase, J. Casanova, and M. B. Plenio, *Phys. Rev. B* **93**, 174104 (2016).
  - [21] J. F. Haase, Z.-Y. Wang, J. Casanova, and M. B. Plenio, *Phys. Rev. Lett.* **121**, 050402 (2018).
  - [22] S. R. Hartmann and E. L. Hahn, *Phys. Rev.* **128**, 2042 (1962).
  - [23] J. Casanova, E. Torrontegui, M. B. Plenio, J. J. García-Ripoll, and E. Solano, *Phys. Rev. Lett.* **122**, 010407 (2019).
  - [24] T. H. Taminiau, J. J. T. Wagenaar, T. van der Sar, F. Jelezko, V. V. Dobrovitski, and R. Hanson, *Phys. Rev. Lett.* **109**, 137602 (2012).
  - [25] J. Casanova, Z.-Y. Wang, J. F. Haase, and M. B. Plenio, *Phys. Rev. A* **92**, 042304 (2015).
  - [26] A. A. Maudsley, *J. Magn. Reson.* **69**, 488 (1986).
  - [27] T. Gullion, D. B. Baker, and M. S. Conradi, *J. Magn. Reson.* **89**, 479 (1990).
  - [28] A. M. Souza, G. A. Álvarez, and D. Suter, *Phys. Rev. Lett.* **106**, 240501 (2011).
  - [29] Z.-Y. Wang, J. Casanova, and M. B. Plenio, *Nat. Commun.* **8**, 14660 (2017).
  - [30] I. Arrazola, J. Casanova, J. S. Pedernales, Z.-Y. Wang, E. Solano, and M. B. Plenio, *Phys. Rev. A* **97**, 052312 (2018).
  - [31] Q.-Y. Cao, Z.-J. Shu, P.-C. Yang, M. Yu, M.-S. Gong, J.-Y. He, R.-F. Hu, A. Retzker, M. B. Plenio, C. Müller, N. Tomek, B. Naydenov, L. P. McGuinness, F. Jelezko, and J.-M. Cai, *arXiv:1710.10744*.
  - [32] M. Loretz, J. M. Boss, T. Rosskopf, H. J. Mamin, D. Rugar, and C. L. Degen, *Phys. Rev. X* **5**, 021009 (2015).
  - [33] J. F. Haase, Z.-Y. Wang, J. Casanova, and M. B. Plenio, *Phys. Rev. A* **94**, 032322 (2016).
  - [34] J. E. Lang, J. Casanova, Z.-Y. Wang, M. B. Plenio, and T. S. Monteiro, *Phys. Rev. Applied* **7**, 054009 (2017).
  - [35] J. Casanova, Z.-Y. Wang, I. Schwartz, and M. B. Plenio, *Phys. Rev. Applied* **10**, 044072 (2018).
  - [36] See Supplemental Material for additional details.
  - [37] A. Ajoy, U. Bissbort, M. D. Lukin, R. L. Walsworth, and P. Cappellaro, *Phys. Rev. X* **5**, 011001 (2015).
  - [38] J. Casanova, Z.-Y. Wang, and M. B. Plenio, *Phys. Rev. Lett.* **117**, 130502 (2016).
  - [39] J. Casanova, Z.-Y. Wang, and M. B. Plenio, *Phys. Rev. A* **96**, 032314 (2017).
  - [40] M. A. Perlin, Z.-Y. Wang, J. Casanova, and M. B. Plenio, *Quantum Sci. Technol.* **4**, 015007 (2018).
  - [41] J.-M. Cai, B. Naydenov, R. Pfeiffer, L. McGuinness, K. D. Jahnke, F. Jelezko, M. B. Plenio, and A. Retzker, *New J. Phys.* **14**, 113023 (2012).

## Supplemental Material: Selective Hybrid Spin Interactions with Low Radiation Power

### I. IDEAL SIGNAL UNDER SINGLE NUCLEAR ADDRESSING

In case of having perfect single nuclear addressing with the  $k$ th nucleus and the  $l$ th harmonic, Eq. (5) in the main text can be reduced to

$$H = \frac{f_l A_k^x}{4} \sigma_z I_k^x. \quad (S1)$$

For the above Hamiltonian the dynamics can be exactly solved, and the evolution of  $\langle \sigma_x \rangle$  (when the initial state is  $\rho = |+\rangle\langle+| \otimes \frac{1}{2}\mathbb{I}$ , i.e. we consider the nucleus in a thermal state) reads

$$\langle \sigma_x \rangle = \cos\left(\frac{f_l A_k^x}{4} t\right). \quad (S2)$$

The above expression represents the depth of each panel (circles or triangles) in Fig. 1. of the main text.

### II. FINDING $\Omega(t)$ FROM $F(t)$

The MW driving in Eq. (2) is  $\frac{\Omega(t)}{2}(|1\rangle\langle 0|e^{i\phi} + \text{H.c.})$ , and its propagator for, e.g., the  $m$ th  $\pi$ -pulse is  $U_t = e^{-i \int_{t_m}^{t_m+t} \frac{\Omega(s)}{2} (|1\rangle\langle 0|e^{i\phi} + \text{H.c.}) ds}$ . During the  $m$ th  $\pi$ -pulse, i.e. in a certain time between  $t_m$  and  $t_m + t$ ,  $U_t$  has the following effect on the electron spin  $\sigma_z$  operator (in the following we call  $\sigma_\phi = |1\rangle\langle 0|e^{i\phi} + \text{H.c.}$ )

$$e^{i \int_{t_m}^{t_m+t} \frac{\Omega(s)}{2} \sigma_\phi ds} \sigma_z e^{-i \int_{t_m}^{t_m+t} \frac{\Omega(s)}{2} \sigma_\phi ds} = e^{i \left( \int_{t_m}^{t_m+t} \Omega(s) ds \right) \sigma_\phi} \sigma_z = \cos\left(\int_{t_m}^{t_m+t} \Omega(s) ds\right) \sigma_z + i \sin\left(\int_{t_m}^{t_m+t} \Omega(s) ds\right) \sigma_\phi \sigma_z. \quad (S3)$$

In this manner, we can say that  $F(t) = \cos\left(\int_{t_m}^{t_m+t} \Omega(s) ds\right)$  while the other spin component, i.e. the one going with  $\sin\left(\int_{t_m}^{t_m+t} \Omega(s) ds\right)$ , does not participate in the joint NV-nucleus dynamics for sequences with alternating pulses [S1] such as the XY-8  $\equiv$  XYXYXYXY pulse sequence we are using in the article. Now, one can easily invert the expression  $F(t) = \cos\left(\int_{t_m}^{t_m+t} \Omega(s) ds\right)$  and find  $\Omega(t) = \frac{\partial}{\partial t} \arccos[F(t)]$ . The latter is the expression mentioned in the main text.

### III. CALCULATION OF $f_l$ COEFFICIENTS

#### A. Coefficients for extended pulses

The analytical expression for the coefficients  $f_l$  is given by

$$f_l = \frac{2}{T} \int_0^T F(s) \cos\left(\frac{2\pi l s}{T}\right) ds, \quad (S4)$$

where  $T = 2\pi/\omega_M$ . With a rescaling of the integrating variable given by  $s = xT/2$ , this is rewritten as

$$f_l = \int_0^2 F(x) \cos(\pi l x) dx. \quad (S5)$$

The function inside the integral is symmetric or antisymmetric w.r.t.  $x = 1$ , depending on  $l$  been odd or even. This can be easily demonstrated by using  $F(x+1) = -F(x)$  and  $\cos(\pi l(x+1)) = \cos(\pi l) \cos \pi l x$ . Thus, if  $l$  is even and the function is symmetric w.r.t  $x = 1$ , the value of the integral will be zero. Anyway, one can work a general expression for Eq.(S5). First, we can divide the integral in two parts,

$$f_l = \int_0^1 F(x) \cos(\pi l x) dx + \int_1^2 F(x) \cos(\pi l x) dx, \quad (S6)$$

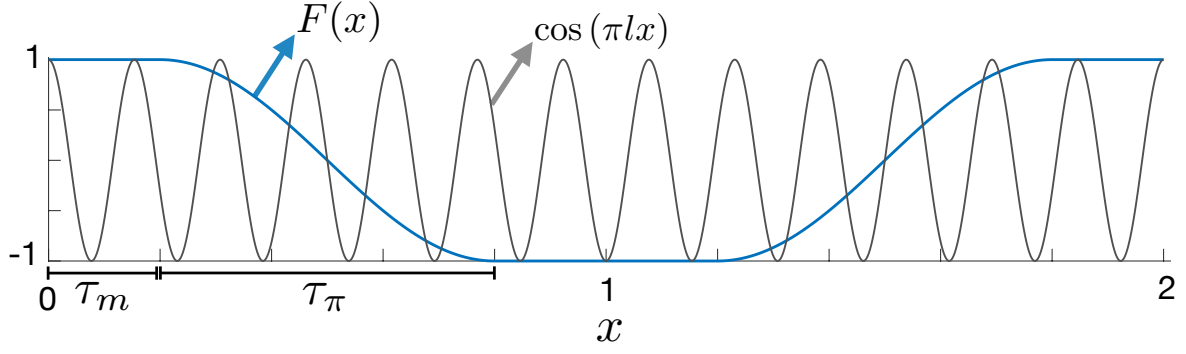


FIG. S1. Plot of  $F(x)$  and  $\cos(\pi lx)$  (where  $l = 13$ ) functions between  $x = 0$  and  $x = 2$ , corresponding to  $t = 0$  and  $t = T$  respectively.

and substitute  $x$  for  $x + 1$  in the second integral. Using the symmetry properties specified above, the equation reduces to

$$f_l = (1 - \cos(\pi l)) \int_0^1 F(x) \cos(\pi lx) dx. \quad (\text{S7})$$

Now, from  $x = 0$  to  $1$ ,  $F(x)$  can be divided in three parts defined by  $\tau_m \equiv 2t_m/T$  and  $1 - \tau_m$ ,

$$f_l = (1 - \cos(\pi l)) \left\{ \int_0^{\tau_m} F(x) \cos(\pi lx) dx + \int_{\tau_m}^{1-\tau_m} F(x) \cos(\pi lx) dx + \int_{1-\tau_m}^1 F(x) \cos(\pi lx) dx \right\}, \quad (\text{S8})$$

and the integral in the middle is zero for the extended pulses. This leaves us with the first and third integrals for which  $F(x)$  is  $1$  and  $-1$  respectively, obtaining

$$f_l^m = (1 - \cos(\pi l)) \left\{ \int_0^{\tau_m} \cos(\pi lx) dx - \int_{1-\tau_m}^1 \cos(\pi lx) dx \right\}, \quad (\text{S9})$$

that leads to

$$f_l^m = \frac{1}{\pi l} (1 - \cos(\pi l)) \left\{ \sin(\pi l \tau_m) + \sin(\pi l (1 - \tau_m)) \right\}. \quad (\text{S10})$$

Using  $\sin(\pi l (1 - \tau_m)) = -\sin(\pi l \tau_m) \cos(\pi l)$  and  $\sin^2 \theta = (1 - \cos(2\theta))/2$ , the expression for  $f_l^m$  reduces to

$$f_l^m = \frac{4}{\pi l} \sin^4(\pi l/2) \sin(\pi l \tau_m). \quad (\text{S11})$$

Now, by using the relation  $T = 4t_m + 2t_\pi$ ,  $f_l^m$  becomes

$$f_l^m = \frac{4}{\pi l} \sin^4(\pi l/2) \sin\left(\pi l \left(\frac{1}{2} + \frac{t_\pi}{T}\right)\right), \quad (\text{S12})$$

where  $t_\pi$  is the duration of a  $\pi$ -pulse. Eq.(S12) is equivalent to Eq.(10) in the main text. To prove that, one may use the trigonometric identity  $\sin(\theta + \pi l/2) = \sin(\theta) \cos(\pi l/2) + \cos(\theta) \sin(\pi l/2)$  which leads us to

$$f_l^m = \frac{4}{\pi l} \cos\left(\pi l \frac{t_\pi}{T}\right) \sin(\pi l/2), \quad (\text{S13})$$

as  $\sin^4(\pi l/2) \cos(\pi l/2) = 0$  and  $\sin^5(\pi l/2) = \sin(\pi l/2)$ . Eq.(S13) is related with Eq.(10) of the main text just by the relation  $\cos(\theta + \pi l) = \cos(\pi l) \cos(\theta)$ .

## B. Coefficients for top-hat pulses

For calculating the value of  $f_l$  coefficients in the case of top-hat pulses, we just need to sum the contribution of the second integral on Eq.(S8), which is not zero for top-hat pulses. The value of  $F(s)$  during the pulse can be written as

$$F(s) = \cos[\pi(s - t_m)/t_\pi], \quad (\text{S14})$$

where  $t_p = t_m + t_\pi/2$ . With the rescaling of the integrating variable introduced in the previous section this is rewritten as

$$F(s) = \cos [\pi(x - \tau_m)/\tau_\pi], \quad (\text{S15})$$

where  $\tau_\pi = 2t_\pi/T$ . So, we need to solve the following integral

$$\int_{\tau_m}^{1-\tau_m} F(x) \cos(\pi l x) dx = \int_{\tau_m}^{1-\tau_m} \cos [\pi(x - \tau_m)/\tau_\pi] \cos(\pi l x) dx \quad (\text{S16})$$

which is not zero. To solve the integral, we can displace the reference frame by a factor of  $\tau_p = 1/2$ , by the change of variable  $x = y + \tau_m + \tau_\pi/2 = y + 1/2$ . Now, the integral will be centered at zero and will look like

$$\int_{-\tau_\pi/2}^{\tau_\pi/2} \cos [\pi y/\tau_\pi + \pi/2] \cos [\pi l(y + 1/2)] dy = - \int_{-\tau_\pi/2}^{\tau_\pi/2} \sin (\pi y/\tau_\pi) \cos [\pi l(y + 1/2)] dy, \quad (\text{S17})$$

and using  $\cos[\pi l(y + 1/2)] = \cos(\pi l y) \cos(\pi l/2) - \sin(\pi l y) \sin(\pi l/2)$  becomes

$$\sin(\pi l/2) \int_{-\tau_\pi/2}^{\tau_\pi/2} \sin(\pi y/\tau_\pi) \sin(\pi l y) dy - \cos(\pi l/2) \int_{-\tau_\pi/2}^{\tau_\pi/2} \sin(\pi y/\tau_\pi) \cos(\pi l y) dy \quad (\text{S18})$$

where the second integral is zero owing to symmetry reasons, i. e.  $\int_{-a}^a F(x) dx = 0$  if  $F(-x) = -F(x)$ . Again, because of symmetry arguments, the first integral is

$$2 \sin(\pi l/2) \int_0^{\tau_\pi/2} \sin(\pi y/\tau_\pi) \sin(\pi l y) dy, \quad (\text{S19})$$

which using trigonometric identities reads

$$\sin(\pi l/2) \left\{ \int_0^{\tau_\pi/2} \cos(\pi y(l - 1/\tau_\pi)) dy - \int_0^{\tau_\pi/2} \cos(\pi y(l + 1/\tau_\pi)) dy \right\} \quad (\text{S20})$$

Solving the integrals one gets

$$\frac{-1}{\pi} \sin(\pi l/2) \cos(\pi l \tau_\pi/2) \left\{ \frac{1}{l - 1/\tau_\pi} + \frac{1}{l + 1/\tau_\pi} \right\}, \quad (\text{S21})$$

which is simplified to

$$\frac{2l\tau_\pi^2}{\pi(1 - l^2\tau_\pi^2)} \sin(\pi l/2) \cos(\pi l \tau_\pi/2). \quad (\text{S22})$$

It is straightforward to prove that the sum of the three integrals in Eq. (S8) gives

$$f_l^{\text{th}} = \frac{4}{\pi l(1 - 4l^2 t_\pi^2/T^2)} \sin(\pi l/2) \cos(\pi l t_\pi/T), \quad (\text{S23})$$

which correspond to the expression written in the main text.

#### IV. ENERGY DELIVERY

The Poynting vector, that describes the energy flux for an electromagnetic wave, is given by

$$\vec{P} = \frac{1}{\mu_0} \vec{E} \times \vec{B}, \quad (\text{S24})$$

where  $\mu_0$  is the vacuum permeability, and  $\vec{E}$  and  $\vec{B}$  are the electric field and magnetic field vectors at the region of interest, i.e. the NV center. The latter, in the nanoscale, is sufficiently small compared with the wavelength of the microwave (MW) radiation to assume a plane wave description of the radiation, so the magnetic field can be written as

$$\vec{B} = \vec{B}_0(t) \cos(\vec{k} \cdot \vec{x} - \omega t + \varphi), \quad (\text{S25})$$



where  $\vec{k}$  is the wavevector and  $\omega$  the frequency of the microwave field. We will also assume an extra time dependence  $B_0(t)$  whose time scales will be several orders of magnitude larger than the period  $2\pi/\omega$ . From Maxwell equations in vacuum it is derived that, for such a magnetic field,  $\vec{k} \cdot \vec{B} = 0$ ,  $\vec{k} \cdot \vec{E} = 0$ , and  $\vec{E} \cdot \vec{B} = 0$ . From the equation  $\vec{\nabla} \times \vec{B} = \frac{1}{c^2} \partial \vec{E} / \partial t$ , it follows that

$$\vec{E} = c^2 \int dt (\vec{\nabla} \times \vec{B}) = -c^2 \int dt (\vec{k} \times \vec{B}_0(t)) \sin(\vec{k} \cdot \vec{x} - \omega t + \varphi). \quad (\text{S26})$$

We choose  $\vec{B}$  to be perpendicular to the NV axis (z axis), specifically, on the x axis. The control Hamiltonian, is then

$$H_c(t) = -\gamma_e \vec{B} \cdot \vec{S} = \gamma_e B_x(t) S_x \cos(\omega t - \phi), \quad (\text{S27})$$

where  $\vec{S}$  corresponds to the spin of the NV center,  $\gamma_e$  is the gyromagnetic ratio of the electron and  $\vec{x} = 0$  the position of the NV. To recover Eq.(1) of the main text, we require that  $\sqrt{2}\Omega(t) = \gamma_e B_x(t)$ . The magnetic field vector at  $\vec{x} = 0$  is then

$$\vec{B}(t) = \frac{\sqrt{2}\Omega(t)}{\gamma_e} \cos(\omega t - \varphi) \hat{x} \quad (\text{S28})$$

and the electric field is, from Eq.(S26),

$$\vec{E}(t) = \frac{\sqrt{2}\omega c}{\gamma_e} \int dt \Omega(t) \sin(\omega t - \varphi) \hat{k} \times \hat{x}, \quad (\text{S29})$$

which, using the wave equation  $\partial^2 \vec{E} / \partial t^2 = c^2 \nabla^2 \vec{E} = \omega^2 \vec{E}$ , converts into

$$\vec{E}(t) = \frac{\sqrt{2}}{k\gamma_e} \frac{\partial}{\partial t} [\Omega(t) \sin(\omega t - \varphi)] \hat{x} \times \hat{k}. \quad (\text{S30})$$

#### A. The case of top-hat $\pi$ pulses

For top-hat pulses we have that  $\partial \Omega(t) / \partial t = 0$ , thus, the energy delivery per unit of area we obtain for top-hat pulses is

$$E^{\text{top-hat}}(t_\pi) = \int_0^{t_\pi} dt |\vec{P}(t)| = \frac{c}{\mu_0} \frac{2}{\gamma_e^2} \int_0^{t_\pi} dt \Omega^2 \cos^2(\omega t - \varphi) = \frac{c}{\mu_0} \frac{\Omega^2}{c\gamma_e^2} \int_0^{t_\pi} dt \{1 + \cos(2\omega t - 2\varphi)\}, \quad (\text{S31})$$

which gives

$$E^{\text{top-hat}}(t_\pi) = \frac{c}{\mu_0} \frac{\Omega^2}{\gamma_e^2} \left\{ t_\pi + \frac{1}{2\omega} \sin(2\omega t - 2\varphi) \right\}. \quad (\text{S32})$$

The second part of the formula is upper bounded by  $(2\omega)^{-1}$ , which, on the other hand, is several orders of magnitude smaller than  $t_\pi$ , thus negligible. As  $t_\pi = \pi/\Omega$ , Eq.(S32) can be rewritten as

$$E^{\text{top-hat}}(t_\pi) \approx \frac{\pi c}{\mu_0} \frac{\Omega}{\gamma_e^2}, \quad (\text{S33})$$

meaning that the energy increases linearly with the Rabi frequency.

#### B. The case of extended $\pi$ pulses

To study the case of an extended  $\pi$  pulse, we need to calculate both terms on Eq.(S30), which are non zero in general. The complete expression is given by

$$E^{\text{extended}}(t_\pi) = \frac{c}{\mu_0} \frac{2}{\gamma_e^2} \int_0^{t_\pi} dt \left[ \Omega^2(t) \cos^2(\omega t - \varphi) + \frac{1}{\omega} \Omega(t) \frac{\partial \Omega(t)}{\partial t} \cos(\omega t - \varphi) \sin(\omega t - \varphi) \right]. \quad (\text{S34})$$

As a final comment, for all cases simulated in the main text we find that the second term at the right hand side of Eq. (S34) is negligible, thus it can be written

$$E^{\text{extended}}(t_\pi) \approx \frac{c}{\mu_0} \frac{2}{\gamma_e^2} \int_0^{t_\pi} dt \left[ \Omega^2(t) \cos^2(\omega t - \varphi) \right]. \quad (\text{S35})$$

### C. Equivalent top-hat Rabi frequency

To calculate the constant Rabi frequency leading to top-hat pulses with the same energy than extended pulses, one has to equal  $E^{\text{top-hat}}(t_\pi) = E^{\text{extended}}(t_\pi)$  and extract the value of the constant  $\Omega$ . With Eqs. (S33, S34) one can easily find that

$$\Omega = \frac{\mu_0 \gamma_e^2}{\pi c} E^{\text{extended}}(t_\pi). \quad (\text{S36})$$

---

[S1] J. E. Lang, J. Casanova, Z.-Y. Wang, M. B. Plenio, and T. S. Monteiro, Phys. Rev. Applied **7**, 054009 (2017).